J. Fluid Mech. (2018), *vol.* 855, *pp.* 860–881. © Cambridge University Press 2018
doi:10.1017/jfm.2018.635

Squeeze flows in liquid films bound by porous disks

David C. Venerus†

Department of Chemical and Biological Engineering and Center for the Molecular Study of Condensed Soft Matter, Illinois Institute of Technology, Chicago, IL 60616, USA

(Received 11 March 2018; revised 21 May 2018; accepted 26 July 2018; first published online 21 September 2018)

Squeeze flows in liquid films between a porous disk and an impermeable disk generated by the relative motion of the disks are analysed. Two configurations that differ by the arrangement of (im)permeable external surfaces that bound the porous disk (i.e. not in contact with the liquid film) are considered. Such configurations allow for bearings with tuneable load-bearing characteristics and are also encountered in joint lubrication, adhesion, printing and composite manufacturing. In the present study, flow in the porous disk is governed by Darcy's law and flow in the liquid film is described using lubrication theory. The present analysis also allows for slip between the liquid film and porous disk. Analytical solutions of the coupled system of equations governing flow in the liquid film and the porous disk are found. Under certain conditions, somewhat unexpected flow patterns are observed in the porous disk. The load-bearing capacity for both configurations is also examined as a function of the permeability and geometry of the permeable disk.

Key words: low-Reynolds-number flows, lubrication theory, porous media

1. Introduction

The hydrodynamics of liquid films between solid surfaces in relative motion has been the subject of investigation since the nineteenth century (Stefan 1874; Reynolds 1886). For incompressible flows of Newtonian fluids in the creeping flow limit, the governing equations (i.e. continuity and Navier–Stokes equations) are linear and allow for analytical solution. For impermeable, parallel, planar disks, it is well known that if the distance between disks decreases linearly with time, then the force on the disk diverges; if a constant force is exerted on one of the disks, then the distance between the disks vanishes only for infinite times. The effect of inertia, which renders the governing equations nonlinear, has been examined by several authors (Jackson 1963; Kuzma 1967; Hamza & Macdonald 1981) using both perturbation and numerical solutions.

Squeeze flows of liquid films are encountered in numerous applications. The most obvious of these include lubrication in thrust bearings (Hamrock, Schmid & Jacobson 2004). Other interesting applications include joint lubrication (e.g. knees and hips), compression moulding of plastics, adhesion, food texture and consumer products.

† Email address for correspondence: venerus@iit.edu

https://doi.org/10.1017/jfm.2018.635 Published online by Cambridge University Press

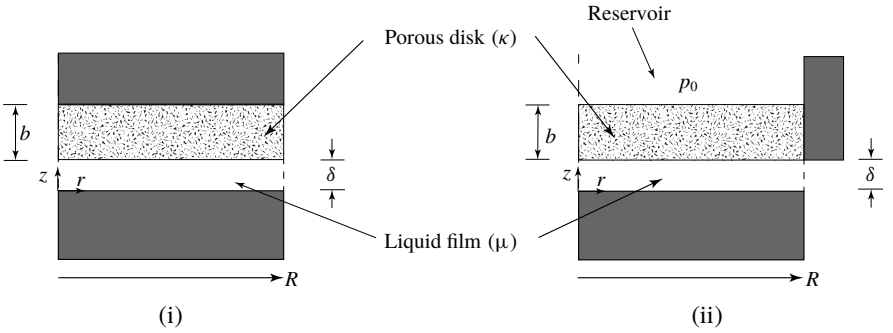


FIGURE 1. Squeezing flow of liquid film between porous and impermeable disks. The porous disk has permeability κ, thickness b and radius R ($\varepsilon = b/R$). For the 'sealed-face' configuration (i) the upper surface of the porous disk is impermeable; for the 'sealed-edge' configuration (ii) the upper surface of the porous disk is permeable and in contact with a reservoir having uniform pressure p_0.

Squeezing flows have also been used to study the rheological behaviour of complex (non-Newtonian) fluids (Engmann, Servais & Burbidge 2005) and soft solids (Meteen 2002; Coussot 2014), which are relevant to many of the applications just mentioned. The dynamics of squeezing liquid films is also important in a rheological technique known as lubricated squeezing flow (Chatraei, Macosko & Winter 1981), which is used to generate equibiaxial elongation deformations in complex fluids. It has been shown that, due to uncontrolled thinning of the low-viscosity liquid films between the sample and the solid disks, lubricated squeezing flow is limited to relatively small strains (Kompani & Venerus 2000; Venerus, Kompani & Bernstein 2000; Guadarrama-Medina, Shiu & Venerus 2009).

Squeezing flows between a solid disk and a porous disk have been investigated because of their relevance to thrust bearings and to the load-bearing characteristics of diathrodial (e.g. knee and hip) joints (Hou *et al.* 1992; Ateshian 2009). The geometry of interest is shown in figure 1 where a liquid film of thickness δ is squeezed between disks of radius R. The lower disk is impermeable while the upper disk with thickness b is porous and has uniform permeability κ. In the 'sealed-face' configuration (i), the upper surface of the porous disk is impermeable and the cylindrical external surface is permeable and exposed to ambient pressure. In the 'sealed-edge' configuration (ii), the cylindrical external surface of the porous disk is impermeable and its upper surface is permeable and in contact with a reservoir having uniform pressure p_0. If p_0 is greater than ambient pressure, liquid flows from the porous disk into the liquid film and configuration (ii) is then referred to as an 'externally pressurized bearing'.

Typically, the equations governing squeezing flows bound by a porous surface are based on Darcy's law to describe flow in the porous medium and the lubrication approximation to describe flow in the liquid film. The latter governs the liquid film pressure, which is a boundary condition for the equation governing the pressure in the porous disk. Hence, the system of equations is coupled. Whereas the no-slip condition is frequently used to describe squeeze flows between impermeable surfaces, a slip velocity is believed to be necessary to formulate boundary conditions at permeable surfaces (Beavers & Joseph 1967), which further couples the governing equations. It is also worth noting for squeezing flows with porous disks that if a constant force is exerted on one of the disks, then the distance between the disks vanishes for finite times.

https://doi.org/10.1017/jfm.2018.635 Published online by Cambridge University Press

The first studies of squeezing flow involving a porous surface considered the sealed-face configuration (i) and use Darcy's law to describe flow in the porous disk. In these studies, squeeze flows show a load-bearing capacity, which depends on the dimensionless parameters $\Psi = \kappa b/\delta^3$ and $\varepsilon = b/R$, that is reduced compared to that of impermeable disks. Wu (1970) and Sparrow, Beavers & Huang (1972) found analytical solutions for the case of a porous annular disk without and with, respectively, a slip velocity. An analytical solution for the case of a porous circular disk without a slip velocity was reported shortly thereafter (Murti 1974*b*). Approximate solutions that include a slip velocity have also been found for annular, circular, rectangular and elliptical porous surfaces (Prakash & Vij 1974). Analytical solutions for rectangular and circular disks with anisotropic permeability have also been reported (Elsharkawy & Nassar 1996). More recently, a perturbation solution valid for small ε for squeezing flow with a porous circular disk has been reported (Knox *et al.* 2015). The same approach has been employed to study the effects of a non-uniform liquid film (Knox *et al.* 2017) and a porous disk with anisotropic permeability (Karmakar & Sekhar 2018). Finally, we note that the effects of fluid viscoelasticity and the elasticity of the porous disk have been considered (Yousefi, Bou-Saïd & Tichy 2015).

A number of studies of squeezing flow involving a porous surface having configuration (i) have used the so-called Brinkman correction to Darcy's law to describe flow in the porous disk (Lin 1996; Lin, Lu & Yang 2001; Nabhani, Khlifi & Bou-Saïd 2010). While this approach may be more general, it introduces additional parameters that are not easily determined. We further note that the Brinkman correction is negligible when the disk porosity is large compared with κ/b^2 (Whitaker 1999).

Squeeze film flows having the sealed-edge configuration (ii) are less well studied. The externally pressurized version of configuration (ii), in contrast to configuration (i), allows the film thickness to be controlled while supporting a given force by supplying liquid to the porous disk from the reservoir. Murti (1974*a*) and Verma (1980) analysed externally pressurized circular bearings with a slip velocity. Approximate analytical solutions were obtained in these studies by assuming that the pressure within the porous disk was a linear function of z, that is, the z-direction pressure gradient was assumed to be independent of z. The validity of this approximation has not been investigated (Murti 1974*a*; Verma 1980), but one would expect it to hold for a thin porous disk ($\varepsilon \ll 1$). A novel modification of the lubricated squeezing flow technique, which addresses the uncontrolled liquid-film thinning issue (Venerus *et al.* 2010), is based on using a porous disk with configuration (ii). Recently, this technique has been used to investigate the rheological behaviour of polymer melts in equibiaxial elongation deformations (Mick, Shiu & Venerus 2015; Mick & Venerus 2017).

In the present study, we investigate squeeze flows in liquid films bound by porous disks. Our primary focus is on the sealed-edge configuration (ii) as only approximate solutions with restricted validity for this case have been reported in the literature. However, since only an approximate solution for porous circular disks with a slip velocity for the sealed-face configuration (i) has been reported, we also present a solution for this case. This allows us to make direct comparisons of the two configurations. In the following section we derive the governing equations for flow in the liquid film and the porous disk and present their solutions for both configurations. This is followed by a presentation and discussion of results where we examine both the flow behaviour in the liquid film and in the porous medium, and investigate the load-bearing characteristics as a function of the porous disk geometry and its permeability. We conclude by summarizing the results of this study.

https://doi.org/10.1017/jfm.2018.635 Published online by Cambridge University Press

2. Problem formulation and solution

We consider the squeezing flow of an incompressible Newtonian fluid with constant density ρ and viscosity μ in a film of thickness $\delta = \delta(t)$ between two disks of radius R (see figure 1). The lower disk is stationary and impermeable; the origin of the coordinate system is fixed to its upper surface. The upper disk with thickness b is porous and has uniform permeability κ. We assume that flow in the porous disk is governed by Darcy's law and, since $\delta \ll R$, that the lubrication approximation holds in the liquid film. There is symmetry about the z-axis and we assume the flow is quasi-stationary. Both gravity and inertia are neglected.

2.1. *General problem*

The velocity in the liquid film is constrained by

$$\frac{1}{r}\frac{\partial}{\partial r}(rv_r) + \frac{\partial v_z}{\partial z} = 0. \tag{2.1}$$

Invoking the lubrication approximation, i.e. neglecting terms $\sim(\delta/R)^2$ and smaller, the r-component of the Navier–Stokes equation takes the form

$$\mu\frac{\partial^2 v_r}{\partial z^2} = \frac{\mathrm{d}p}{\mathrm{d}r}, \tag{2.2}$$

where we have $p = p(r)$. Boundary conditions at the impermeable disk are given by

$$v_r(r, 0) = 0, \quad v_z(r, 0) = 0, \tag{2.3a,b}$$

and at the permeable disk by

$$v_r(r, \delta) = \langle v_r\rangle_s(r, \delta) - \frac{\sqrt{\kappa}}{\alpha}\frac{\partial v_r}{\partial z}(r, \delta), \quad v_z(r, \delta) = \langle v_z\rangle_s(r, \delta) + \dot{\delta}, \tag{2.4a,b}$$

where $\langle \boldsymbol{v}\rangle_s$ is the superficial average velocity in the porous disk (Whitaker 1999). The first boundary condition in (2.4), for finite values of the dimensionless parameter α, allows for 'slip' between the liquid and porous disk (Beavers & Joseph 1967), and in the second boundary condition $\dot{\delta} = \mathrm{d}\delta/\mathrm{d}t$.

Integration of (2.2) with respect to z and applying the boundary conditions in (2.3*a*) and (2.4*a*) gives

$$v_r = -\frac{\delta^2}{2\mu}\frac{\mathrm{d}p}{\mathrm{d}r}\left[\frac{1+2\sigma}{1+\sigma}\frac{z}{\delta} - \left(\frac{z}{\delta}\right)^2\right] + \frac{\langle v_r\rangle_s(r, \delta)}{1+\sigma}\frac{z}{\delta}, \tag{2.5}$$

where $\sigma = \sqrt{\kappa}/\alpha\delta$. Substitution of (2.5) in (2.1) gives

$$\frac{\partial v_z}{\partial z} = \frac{\delta^2}{2\mu}\frac{1}{r}\frac{\mathrm{d}}{\mathrm{d}r}\left(r\frac{\mathrm{d}p}{\mathrm{d}r}\right)\left[\frac{1+2\sigma}{1+\sigma}\frac{z}{\delta} - \left(\frac{z}{\delta}\right)^2\right] - \frac{1}{1+\sigma}\frac{1}{r}\frac{\partial}{\partial r}\left(r\langle v_r\rangle_s(r, \delta)\right)\frac{z}{\delta}. \tag{2.6}$$

Integration of (2.6) over z from 0 to δ with the boundary conditions in (2.3*b*) and (2.4*b*) gives

$$\frac{1}{r}\frac{\mathrm{d}}{\mathrm{d}r}\left(r\frac{\mathrm{d}p}{\mathrm{d}r}\right) = 12\frac{1+\sigma}{1+4\sigma}\frac{\mu}{\delta^3}[\dot{\delta} + \langle v_z\rangle_s(r, \delta)] + \frac{6}{1+4\sigma}\frac{\mu}{\delta^2}\frac{1}{r}\frac{\partial}{\partial r}(r\langle v_r\rangle_s(r, \delta)), \tag{2.7}$$

https://doi.org/10.1017/jfm.2018.635 Published online by Cambridge University Press

which is the Reynolds equation for the liquid film. We note that the stress from (2.6) is $(\delta/R)^2$ times smaller than the stress from (2.7).

The superficial average velocity $\langle \boldsymbol{v} \rangle_s$ in the porous disk is constrained by

$$\frac{1}{r}\frac{\partial}{\partial r}(r\langle v_r\rangle_s) + \frac{\partial \langle v_z\rangle_s}{\partial z} = 0. \tag{2.8}$$

The superficial average streamfunction $\langle \psi \rangle_s$ is defined by the relations

$$\langle v_r\rangle_s = -\frac{1}{r}\frac{\partial \langle \psi\rangle_s}{\partial z}, \quad \langle v_z\rangle_s = \frac{1}{r}\frac{\partial \langle \psi\rangle_s}{\partial r}. \tag{2.9a,b}$$

We assume flow in the porous disk is governed by Darcy's law, which takes the form

$$\langle v_r\rangle_s = -\frac{\kappa}{\mu}\frac{\partial \langle p\rangle_i}{\partial r}, \quad \langle v_z\rangle_s = -\frac{\kappa}{\mu}\frac{\partial \langle p\rangle_i}{\partial z}, \tag{2.10a,b}$$

where $\langle p \rangle_i$ is the intrinsic average pressure within the porous disk (Whitaker 1999). Combining (2.8) and (2.10), we have

$$\frac{1}{r}\frac{\partial}{\partial r}\left(r\frac{\partial \langle p\rangle_i}{\partial r}\right) + \frac{\partial^2 \langle p\rangle_i}{\partial z^2} = 0, \tag{2.11}$$

which is solved subject to $\partial \langle p\rangle_i/\partial r(0, z) = 0$ and the boundary condition

$$\langle p\rangle_i(r, \delta) = p(r). \tag{2.12}$$

Using (2.10) and (2.11), we can write (2.7) as

$$\frac{1}{r}\frac{\mathrm{d}}{\mathrm{d}r}\left(r\frac{\mathrm{d}p}{\mathrm{d}r}\right) = 12\frac{1+\sigma}{1+4\sigma}\frac{\mu\dot{\delta}}{\delta^3} - 12\frac{1+\sigma}{1+4\sigma}\frac{\kappa}{\delta^3}\frac{\partial \langle p\rangle_i}{\partial z}(r, \delta) + \frac{6}{1+4\sigma}\frac{\kappa}{\delta^2}\frac{\partial^2 \langle p\rangle_i}{\partial z^2}(r, \delta), \tag{2.13}$$

which is solved subject to $\mathrm{d}p/\mathrm{d}r(0) = 0$ and $p(R) = 0$. The coupled system of (2.11)–(2.13) applies to both configurations (i) and (ii). To solve (2.11) for $\langle p \rangle_i$, additional boundary conditions must be prescribed.

Finally, the force exerted by the liquid film on the porous disk is obtained from

$$\mathcal{F} = 2\pi \int_0^R p(r) r\,\mathrm{d}r, \tag{2.14}$$

where, as noted previously, we are neglecting terms from (2.6) that are $(\delta/R)^2$ times smaller than those being retained.

2.2. *Solution for the sealed-face configuration (i)*

First, we consider the sealed-face configuration (i) shown in figure 1 for which the boundary conditions for (2.11) are

$$\frac{\partial \langle p\rangle_i}{\partial z}(r, \delta + b) = 0, \tag{2.15}$$

$$\langle p\rangle_i(R, z) = 0. \tag{2.16}$$

https://doi.org/10.1017/jfm.2018.635 Published online by Cambridge University Press

The solution to (2.11) subject to (2.12), (2.15) and (2.16) can be written as

$$\langle p\rangle_i = \sum_{n=1}^{\infty} B_n \frac{\mathrm{J}_0(\beta_n r)\cosh[\beta_n(\delta+b-z)]}{\cosh(\beta_n b)}, \tag{2.17}$$

where $\mathrm{J}_0(x)$ is the Bessel function of the first kind. The β_n are found from the roots of $\mathrm{J}_0(\beta_n R)=0$, $n=1, 2, 3, \ldots$, and

$$B_n = \frac{2}{R^2\mathrm{J}_1^2(\beta_n R)}\int_0^R p(r)\mathrm{J}_0(\beta_n r) r\,\mathrm{d}r, \quad n=1, 2, 3, \ldots. \tag{2.18}$$

Substituting (2.17) in (2.13), we obtain

$$\frac{1}{r}\frac{\mathrm{d}}{\mathrm{d}r}\left(r\frac{\mathrm{d}p}{\mathrm{d}r}\right) = 12\frac{1+\sigma}{1+4\sigma}\frac{\mu\dot{\delta}}{\delta^3} + \frac{12}{1+4\sigma}\frac{\kappa}{\delta^3}\sum_{n=1}^{\infty} B_n\left[(1+\sigma)\tanh(\beta_n b)+\frac{1}{2}\delta\beta_n\right]\beta_n\mathrm{J}_0(\beta_n r). \tag{2.19}$$

Integrating (2.19) twice with respect to r gives

$$p = -3\frac{1+\sigma}{1+4\sigma}\mu\frac{R^2}{\delta^3}\dot{\delta}\left[1-\left(\frac{r}{R}\right)^2\right] - \frac{12}{1+4\sigma}\frac{\kappa R}{\delta^3}\sum_{n=1}^{\infty} B_n\left[(1+\sigma)\frac{\tanh(\beta_n b)}{\beta_n R}+\frac{1}{2}\frac{\delta}{R}\right]\mathrm{J}_0(\beta_n r). \tag{2.20}$$

Substitution of (2.20) in (2.18) gives

$$B_n = -24\frac{1+\sigma}{1+4\sigma}\mu\dot{\delta}\frac{R^2}{\delta^3}\frac{1}{(\beta_n R)^3\mathrm{J}_1(\beta_n R)}\left\{1+\frac{12}{1+4\sigma}\frac{\kappa R}{\delta^3}\left[(1+\sigma)\frac{\tanh(\beta_n b)}{\beta_n R}+\frac{1}{2}\frac{\delta}{R}\right]\right\}^{-1}. \tag{2.21}$$

Substituting (2.21) in (2.20) we obtain

$$\frac{p\delta^3}{\mu R^2} = -3\frac{1+\sigma}{1+4\sigma}\dot{\delta}\sum_{n=1}^{\infty}\frac{8}{\bar{\beta}_n^3}\left\{1+\frac{12\Upsilon}{1+4\sigma}\left[(1+\sigma)\frac{\tanh(\bar{\beta}_n\varepsilon)}{\bar{\beta}_n}+\frac{1}{2}\frac{\delta}{R}\right]\right\}^{-1}\frac{\mathrm{J}_0(\bar{\beta}_n r/R)}{\mathrm{J}_1(\bar{\beta}_n)}, \tag{2.22}$$

where $\bar{\beta}_n=\beta_n R$, $\varepsilon=b/R$ and $\Upsilon=\kappa R/\delta^3$ (note that $\Upsilon=\Psi/\varepsilon$). Substituting (2.21) in (2.17) we obtain

$$\begin{aligned}\frac{\langle p\rangle_i\delta^3}{\mu R^2} &= -3\frac{1+\sigma}{1+4\sigma}\dot{\delta}\sum_{n=1}^{\infty}\frac{8}{\bar{\beta}_n^3}\left\{1+\frac{12\Upsilon}{1+4\sigma}\left[(1+\sigma)\frac{\tanh(\bar{\beta}_n\varepsilon)}{\bar{\beta}_n}+\frac{1}{2}\frac{\delta}{R}\right]\right\}^{-1}\\ &\quad\times\frac{\mathrm{J}_0(\bar{\beta}_n r/R)\cosh\left(\bar{\beta}_n\varepsilon[1-(z-\delta)/b]\right)}{\mathrm{J}_1(\bar{\beta}_n)\cosh(\bar{\beta}_n\varepsilon)},\end{aligned} \tag{2.23}$$

and from (2.5) using (2.22) and (2.23), we find

$$\begin{aligned}\frac{v_r\delta}{R} &= -\frac{12}{1+4\sigma}\dot{\delta}\left[\left(1+2\sigma+2\frac{\delta}{R}\Upsilon\right)\frac{z}{\delta}-(1+\sigma)\left(\frac{z}{\delta}\right)^2\right]\\ &\quad\times\sum_{n=1}^{\infty}\left\{1+\frac{12\Upsilon}{1+4\sigma}\left[(1+\sigma)\frac{\tanh(\bar{\beta}_n\varepsilon)}{\bar{\beta}_n}+\frac{1}{2}\frac{\delta}{R}\right]\right\}^{-1}\frac{\mathrm{J}_1(\bar{\beta}_n r/R)}{\bar{\beta}_n^2\mathrm{J}_1(\bar{\beta}_n)}.\end{aligned} \tag{2.24}$$

https://doi.org/10.1017/jfm.2018.635 Published online by Cambridge University Press

Using (2.23) with (2.10) and (2.9) we obtain

$$\frac{\langle\psi\rangle_s}{R^2} = -3\dot{\delta}\frac{1+\sigma}{1+4\sigma}\Upsilon\sum_{n=1}^{\infty}\frac{8}{\bar{\beta}_n^3}\left\{1+\frac{12\Upsilon}{1+4\sigma}\left[(1+\sigma)\frac{\tanh(\bar{\beta}_n\varepsilon)}{\bar{\beta}_n}+\frac{1}{2}\frac{\delta}{R}\right]\right\}^{-1} \times\frac{(r/R)\mathrm{J}_1(\bar{\beta}_n r/R)\sinh\left(\bar{\beta}_n\varepsilon[1-(z-\delta)/b]\right)}{\mathrm{J}_1(\bar{\beta}_n)\cosh(\bar{\beta}_n\varepsilon)}. \tag{2.25}$$

Finally, substituting (2.22) in (2.14) we obtain

$$\frac{2\mathcal{F}}{3\mu\pi R^4} = -\frac{1+\sigma}{1+4\sigma}\frac{\dot{\delta}}{\delta^3}\sum_{n=1}^{\infty}\frac{32}{\bar{\beta}_n^4}\left\{1+\frac{12\Upsilon}{1+4\sigma}\left[(1+\sigma)\frac{\tanh(\bar{\beta}_n\varepsilon)}{\bar{\beta}_n}+\frac{1}{2}\frac{\delta}{R}\right]\right\}^{-1}, \tag{2.26}$$

(note that $\sum_{n=1}^{\infty} 32/\bar{\beta}_n^4 = 1$). For the no-slip case ($\sigma = 0$), the expressions in (2.22) and (2.26) simplify to those given by Murti (1974*b*).

2.3. *Solution for the sealed-edge configuration (ii)*

For the sealed-edge configuration (ii) shown in figure 1, we have the boundary conditions

$$\langle p\rangle_i(r,\,\delta+b) = p_0, \tag{2.27}$$

$$\frac{\partial\langle p\rangle_i}{\partial r}(R,\,z) = 0. \tag{2.28}$$

The solution of (2.11) subject to (2.12), (2.27) and (2.28) can be written as

$$\langle p\rangle_i = p_0 + (p_0-\bar{p})\left(\frac{z-\delta}{b}-1\right)+\sum_{n=1}^{\infty}A_n\frac{\mathrm{J}_0(\alpha_n r)\sinh[\alpha_n(\delta+b-z)]}{\sinh[\alpha_n b]}, \tag{2.29}$$

where

$$\bar{p} = \frac{2}{R^2}\int_0^R p(r)r\,\mathrm{d}r \tag{2.30}$$

is the average pressure in the liquid film. The α_n are found from the roots of $\mathrm{J}_1(\alpha_n R) = 0$, $n = 0, 1, 2, \ldots$, which includes $\alpha_0 = 0$, and the A_n are given by

$$A_n = \frac{2}{R^2\mathrm{J}_0^2(\alpha_n R)}\int_0^R p(r)\mathrm{J}_0(\alpha_n r)r\,\mathrm{d}r, \quad n = 1, 2, 3, \ldots. \tag{2.31}$$

The total mass flow rate $\mathcal{W}$ from the reservoir to the porous disk is given by

$$\frac{\mathcal{W}}{\rho\pi} = -2\int_0^R\langle v_z\rangle_s(r,\,b+\delta)r\,\mathrm{d}r = \frac{\kappa R^2}{\mu b}(p_0-\bar{p}), \tag{2.32}$$

where the second equality is obtained using (2.10*b*) and (2.29).

Substitution of (2.29) in (2.13) leads to

$$\frac{1}{r}\frac{\mathrm{d}}{\mathrm{d}r}\left(r\frac{\mathrm{d}p}{\mathrm{d}r}\right) = 12\frac{1+\sigma}{1+4\sigma}\frac{\mu}{\delta^3}\left[\dot{\delta}-\frac{\kappa}{\mu b}(p_0-\bar{p})\right] - \frac{12}{1+4\sigma}\frac{\kappa}{\delta^3}\sum_{n=1}^{\infty}A_n\left[(1+\sigma)\coth(\alpha_n b)+\frac{1}{2}\delta\alpha_n\right]\alpha_n\mathrm{J}_0(\alpha_n r). \tag{2.33}$$

https://doi.org/10.1017/jfm.2018.635 Published online by Cambridge University Press

Integrating (2.33) twice with respect to r gives

$$p = -3\frac{1+\sigma}{1+4\sigma}\mu\frac{R^2}{\delta^3}\left[\dot{\delta}-\frac{\kappa}{\mu b}(p_0-\bar{p})\right]\left[1-\left(\frac{r}{R}\right)^2\right] + \frac{12}{1+4\sigma}\frac{\kappa R}{\delta^3}\sum_{n=1}^{\infty}A_n\left[(1+\sigma)\frac{\coth(\alpha_n b)}{\alpha_n R}+\frac{1}{2}\frac{\delta}{R}\right][\mathrm{J}_0(\alpha_n R)-\mathrm{J}_0(\alpha_n r)]. \quad (2.34)$$

Substitution of (2.34) in (2.31) gives

$$A_n = 12\frac{1+\sigma}{1+4\sigma}\mu\frac{R^2}{\delta^3}\left(\dot{\delta}-\frac{\mathcal{W}}{\rho\pi R^2}\right)\frac{1}{(\alpha_n R)^2\mathrm{J}_0(\alpha_n R)} \times\left\{1+\frac{12}{1+4\sigma}\frac{\kappa R}{\delta^3}\left[(1+\sigma)\frac{\coth(\alpha_n b)}{\alpha_n R}+\frac{1}{2}\frac{\delta}{R}\right]\right\}^{-1}, \quad (2.35)$$

where (2.32) has been used. Using (2.34) and (2.35), the pressure in the liquid film is given by

$$\frac{p\delta^3}{\mu R^2} = -3\frac{1+\sigma}{1+4\sigma}\left(\dot{\delta}-\frac{\mathcal{W}}{\rho\pi R^2}\right)\sum_{n=1}^{\infty}\frac{4}{\bar{\alpha}_n^2}\left\{1+\frac{12\Upsilon}{1+4\sigma}\left[(1+\sigma)\frac{\coth(\bar{\alpha}_n\varepsilon)}{\bar{\alpha}_n}+\frac{1}{2}\frac{\delta}{R}\right]\right\}^{-1} \times\left[1-\frac{\mathrm{J}_0(\bar{\alpha}_n r/R)}{\mathrm{J}_0(\bar{\alpha}_n)}\right], \quad (2.36)$$

where $\bar{\alpha}_n = \alpha_n R$. Combining (2.30), (2.32) and (2.36), p_0 is given by

$$\frac{p_0\delta^3}{\mu R^2} = \frac{\mathcal{W}}{\rho\pi R^2}\frac{\varepsilon}{\Upsilon}-\frac{3}{2}\frac{1+\sigma}{1+4\sigma}\left(\dot{\delta}-\frac{\mathcal{W}}{\rho\pi R^2}\right)\sum_{n=1}^{\infty}\frac{8}{\bar{\alpha}_n^2} \times\left\{1+\frac{12\Upsilon}{1+4\sigma}\left[(1+\sigma)\frac{\coth(\bar{\alpha}_n\varepsilon)}{\bar{\alpha}_n}+\frac{1}{2}\frac{\delta}{R}\right]\right\}^{-1}. \quad (2.37)$$

To obtain $\langle p\rangle_i$, (2.32), (2.35) and (2.37) are substituted in (2.29), which gives

$$\frac{\langle p\rangle_i\delta^3}{\mu R^2} = \frac{\mathcal{W}}{\rho\pi R^2}\frac{\varepsilon}{\Upsilon}\frac{z-\delta}{b}-\frac{3}{2}\frac{1+\sigma}{1+4\sigma}\left(\dot{\delta}-\frac{\mathcal{W}}{\rho\pi R^2}\right) \times\sum_{n=1}^{\infty}\frac{8}{\bar{\alpha}_n^2}\left\{1+\frac{12\Upsilon}{1+4\sigma}\left[(1+\sigma)\frac{\coth(\bar{\alpha}_n\varepsilon)}{\bar{\alpha}_n}+\frac{1}{2}\frac{\delta}{R}\right]\right\}^{-1} \times\left[1-\frac{\mathrm{J}_0(\bar{\alpha}_n r/R)\sinh(\bar{\alpha}_n\varepsilon[1-(z-\delta)/b])}{\mathrm{J}_0(\bar{\alpha}_n)\sinh(\bar{\alpha}_n\varepsilon)}\right]. \quad (2.38)$$

From (2.5) using (2.36) and (2.38), we find

$$\frac{v_r\delta}{R} = \frac{6}{1+4\sigma}\left(\dot{\delta}-\frac{\mathcal{W}}{\rho\pi R^2}\right)\left[\left(1+2\sigma+2\frac{\delta}{R}\Upsilon\right)\frac{z}{\delta}-(1+\sigma)\left(\frac{z}{\delta}\right)^2\right] \times\sum_{n=1}^{\infty}\left\{1+\frac{12\Upsilon}{1+4\sigma}\left[(1+\sigma)\frac{\coth(\bar{\alpha}_n\varepsilon)}{\bar{\alpha}_n}+\frac{1}{2}\frac{\delta}{R}\right]\right\}^{-1}\frac{\mathrm{J}_1(\bar{\alpha}_n r/R)}{\bar{\alpha}_n\mathrm{J}_0(\bar{\alpha}_n)}. \quad (2.39)$$

https://doi.org/10.1017/jfm.2018.635 Published online by Cambridge University Press

Using (2.38) with (2.10) and (2.9) we obtain

$$\frac{\langle\psi\rangle_s}{R^2} = -\frac{1}{2}\frac{\mathcal{W}}{\rho\pi R^2}\left(\frac{r}{R}\right)^2 + \frac{3}{2}\frac{1+\sigma}{1+4\sigma}\Upsilon\left(\dot{\delta} - \frac{\mathcal{W}}{\rho\pi R^2}\right) \times \sum_{n=1}^{\infty}\frac{8}{\bar{\alpha}_n^2}\left\{1 + \frac{12\Upsilon}{1+4\sigma}\left[(1+\sigma)\frac{\tanh(\bar{\alpha}_n\varepsilon)}{\bar{\alpha}_n} + \frac{1}{2}\frac{\delta}{R}\right]\right\}^{-1} \times \frac{(r/R)\mathrm{J}_1(\bar{\alpha}_n r/R)\cosh\left(\bar{\alpha}_n\varepsilon[1-(z-\delta)/b]\right)}{\mathrm{J}_0(\bar{\alpha}_n)\sinh(\bar{\alpha}_n\varepsilon)}. \tag{2.40}$$

Substitution of (2.36) in (2.14) gives

$$\frac{2\mathcal{F}}{3\mu\pi R^4} = -\frac{1+\sigma}{1+4\sigma}\frac{1}{\delta^3}\left(\dot{\delta} - \frac{\mathcal{W}}{\rho\pi R^2}\right)\sum_{n=1}^{\infty}\frac{8}{\bar{\alpha}_n^2} \times \left\{1 + \frac{12\Upsilon}{1+4\sigma}\left[(1+\sigma)\frac{\coth(\bar{\alpha}_n\varepsilon)}{\bar{\alpha}_n} + \frac{1}{2}\frac{\delta}{R}\right]\right\}^{-1} \tag{2.41}$$

(note that $\sum_{n=1}^{\infty} 8/\bar{\alpha}_n^2 = 1$).

We consider two cases for configuration (ii). One is the externally pressurized bearing case where the mass flow rate from the reservoir to the porous disk $\mathcal{W}$ is prescribed. The other case is when the reservoir pressure is equal to the ambient pressure ($p_0 = 0$) so that, similar to configuration (i), liquid flows from the porous disk at a permeable external surface. In this case, from (2.37), $\mathcal{W}$ is found to be

$$\frac{\mathcal{W}}{\rho\pi R^2} = \dot{\delta}\left[1 - \left(1 + \frac{3}{2}\frac{1+\sigma}{1+4\sigma}\frac{\Upsilon}{\varepsilon}\sum_{n=1}^{\infty}\frac{8}{\bar{\alpha}_n^2} \times \left\{1 + \frac{12\Upsilon}{1+4\sigma}\left[(1+\sigma)\frac{\coth(\bar{\alpha}_n\varepsilon)}{\bar{\alpha}_n} + \frac{1}{2}\frac{\delta}{R}\right]\right\}^{-1}\right)^{-1}\right]. \tag{2.42}$$

Note that for squeezing flow $\dot{\delta} < 0$ we have $\mathcal{W} < 0$, i.e. liquid flows from the porous disk to the reservoir $[(..)^{-1} = 1 - \mathcal{W}/\rho\pi R^2\dot{\delta}]$. Substitution of (2.42) in (2.41) gives

$$\frac{2\mathcal{F}}{3\mu\pi R^4} = -\frac{1+\sigma}{1+4\sigma}\frac{\dot{\delta}}{\delta^3} \times \left(1 + \frac{3}{2}\frac{1+\sigma}{1+4\sigma}\frac{\Upsilon}{\varepsilon}\sum_{n=1}^{\infty}\frac{8}{\bar{\alpha}_n^2}\left\{1 + \frac{12\Upsilon}{1+4\sigma}\left[(1+\sigma)\frac{\coth(\bar{\alpha}_n\varepsilon)}{\bar{\alpha}_n} + \frac{1}{2}\frac{\delta}{R}\right]\right\}^{-1}\right)^{-1} \times \sum_{n=1}^{\infty}\frac{8}{\bar{\alpha}_n^2}\left\{1 + \frac{12\Upsilon}{1+4\sigma}\left[(1+\sigma)\frac{\coth(\bar{\alpha}_n\varepsilon)}{\bar{\alpha}_n} + \frac{1}{2}\frac{\delta}{R}\right]\right\}^{-1}. \tag{2.43}$$

3. Results and discussion

From the previous section we see that squeeze flow in liquid films bound by a porous disk involves four dimensionless quantities. These include the aspect ratios of the porous disk $\varepsilon = b/R$ and lubricant film thickness δ/R. The latter is typically

https://doi.org/10.1017/jfm.2018.635 Published online by Cambridge University Press

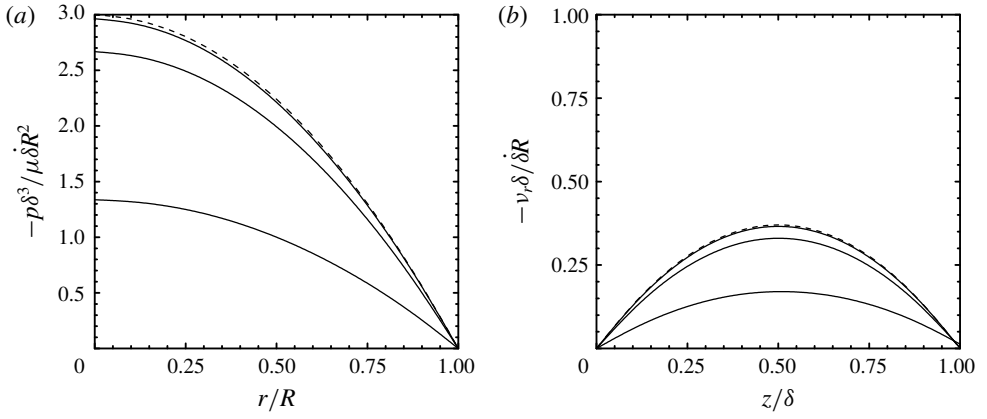


FIGURE 2. Pressure (a) from (2.22) and radial velocity at $r/R = 0.5$ (b) from (2.24) in liquid film for configuration (i) with constant squeezing velocity $-\dot{\delta}$ for different values of permeability parameter $\Upsilon = \kappa R/\delta^3 = 0.01, 0.1, 1.0$ (solid lines top to bottom) with $\varepsilon = 0.1$, $\delta/R = 0.01$ and $\sigma = 0$. The dashed line is for the impermeable disk.

small so we set $\delta/R = 0.01$ for all results in this section. The remaining dimensionless parameters are for slip $\sigma = \kappa/\alpha\delta$ and disk permeability $\Upsilon = \kappa R/\delta^3$, both of which vanish for the case of an impermeable disk ($\kappa = 0$). We begin by presenting results for the velocity and pressure fields in the liquid film and porous disk. This is followed by results illustrating the load-bearing behaviour of the two configurations.

3.1. *Velocity and pressure fields*

First, we consider the sealed-face configuration (i). Figure 2 shows the pressure and radial velocity fields in the liquid film for constant squeeze velocity $-\dot{\delta}$. For the impermeable disk case ($\sigma = \Upsilon = 0$), the expression in (2.22) gives $p \propto [1 - (r/R)^2]$ and the expression in (2.24) gives $v_r \propto (r/R)[(z/\delta) - (z/\delta)^2]$. From this figure we see that the pressure profile flattens, which, in turn, leads to a reduction in the radial velocity, as the permeability of the disk Υ increases. Pressure and streamfunction contours within the porous disk are presented in figure 3, which shows that liquid flows into the porous disk axially and then, because of the impermeable upper surface, flows in the radial direction.

We now examine the sealed-edge configuration (ii) for the case where $p_0 = 0$ so that liquid flows from the porous disk to the reservoir. Again, for the impermeable disk case ($\sigma = \Upsilon = 0$), the expression in (2.36) simplifies to $p \propto [1 - (r/R)^2]$ and the expression in (2.39) simplifies to $v_r \propto (r/R)[(z/\delta) - (z/\delta)^2]$. Figure 4 shows the pressure and radial velocity fields in the liquid film for constant squeeze velocity $-\dot{\delta}$. As with configuration (i), the pressure profile flattens and the radial velocity decreases as Υ increases; however, the dependence on Υ is stronger for configuration (ii) compared to configuration (i). For large permeability ($\Upsilon = 1.0$), the liquid-film pressure is nearly uniform and the radial velocity approaches zero.

As noted earlier, approximate solutions for configuration (ii) have been reported (Murti 1974*a*; Verma 1980) by assuming $\langle p \rangle_i$ is a linear function of z. In this case, the pressure within the porous disk is found using the boundary conditions in (2.12) and (2.27) and is given by $\langle p \rangle_i = p_0 + (p_0 - p)[(z - \delta)/b - 1]$. We note, however, that

https://doi.org/10.1017/jfm.2018.635 Published online by Cambridge University Press

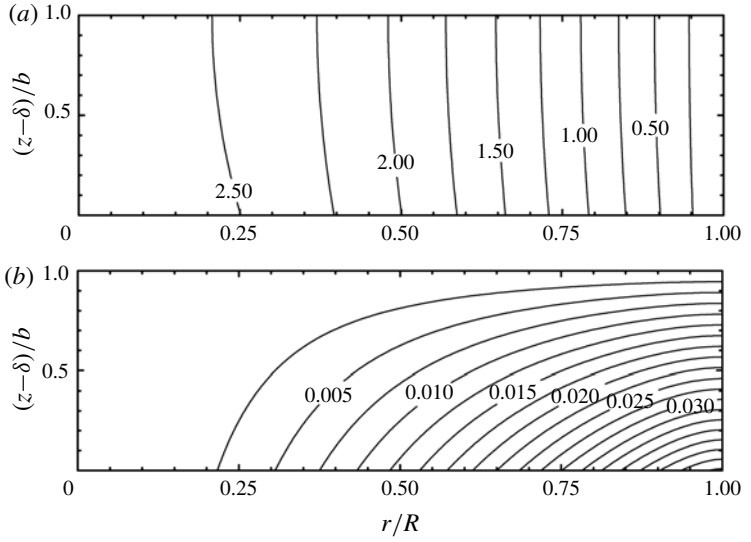


FIGURE 3. Pressure (*a*) $-\langle p\rangle_i \delta^3/\mu\dot{\delta}R^2$ from (2.23) and streamfunction (*b*) $-\langle\psi\rangle_s/\dot{\delta}R^2$ from (2.25) contours in a porous disk for configuration (i) with constant squeezing velocity $-\dot{\delta}$ for permeability parameter $\Upsilon = \kappa R/\delta^3 = 0.1$ with $\varepsilon = 0.1$, $\delta/R = 0.01$ and $\sigma = 0$.

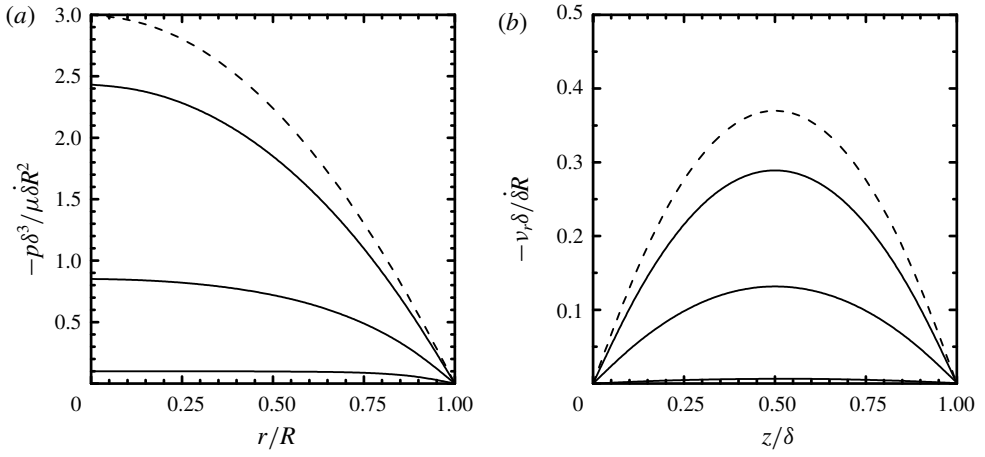


FIGURE 4. Pressure (*a*) from (2.36) and radial velocity at $r/R = 0.5$ (*b*) from (2.39) for configuration (ii) with constant squeezing velocity $-\dot{\delta}$ for different values of permeability parameter $\Upsilon = \kappa R/\delta^3 = 0.01$, 0.1, 1.0 (solid lines top to bottom) with $\varepsilon = 0.1$, $\delta/R = 0.01$ and $\sigma = 0$. The dashed line is for the impermeable disk.

this solution is not consistent with (2.8), (2.10*a*) and (2.10*b*). Nevertheless, using this assumption (and setting $p_0 = 0$, $\sigma = 0$) the solution of (2.13) can be written as

$$\frac{p\delta^3}{\mu R^2} = -\dot{\delta}\frac{\varepsilon}{\Upsilon}\left[1 - \frac{\mathrm{I}_0(\sqrt{12\Upsilon/\varepsilon}\,r/R)}{\mathrm{I}_0(\sqrt{12\Upsilon/\varepsilon})}\right], \tag{3.1}$$

https://doi.org/10.1017/jfm.2018.635 Published online by Cambridge University Press

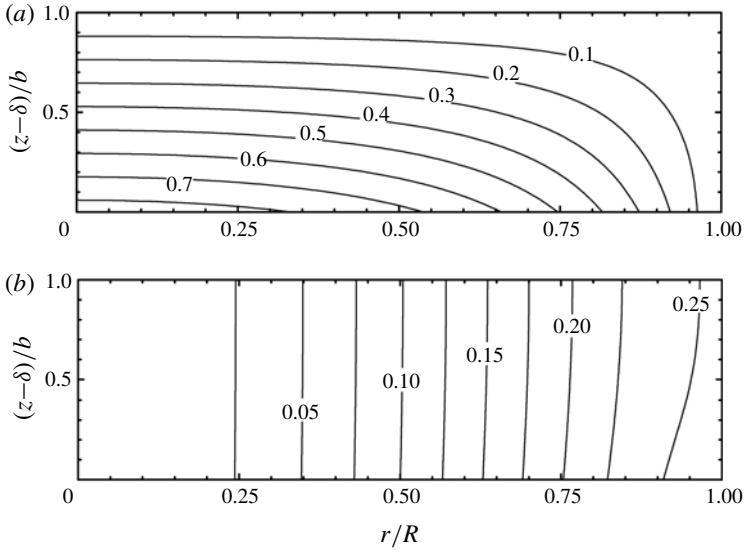


FIGURE 5. Pressure (*a*) $-\langle p\rangle_i\delta^3/\mu\dot{\delta}R^2$ from (2.38) and streamfunction (*b*) $-\langle\psi\rangle_s/\dot{\delta}R^2$ from (2.40) contours in a porous disk for configuration (ii) with constant squeezing velocity $-\dot{\delta}$ for permeability parameter $\Upsilon=\kappa R/\delta^3=0.1$ with $\varepsilon=0.1$, $\delta/R=0.01$ and $\sigma=0$.

where $\mathrm{I}_0(x)$ is the modified Bessel function of the first kind. This expression is in good agreement with (2.36) for $\varepsilon\ll 1$, but over-predicts the liquid-film pressure for larger ε.

Pressure and streamfunction contours within the porous disk for configuration (ii) are presented in figure 5. From this figure we see that flow in the porous disk is mainly in the axial direction except near the outer edge of the disk. The detailed view given in figure 6 shows the flow splits where a portion of the liquid (for $r/R\gtrsim 0.93$) entering the porous disk from the film flows back into the film, that is $\langle v_z\rangle_s(r,\delta)<0$. This occurs because liquid flow in the radial direction encounters the impermeable surface at $r=R$, which results in a stagnation point. Hence, the flow resistance along a path back to liquid film is smaller than along a path through the porous disk to the reservoir. Pressure and streamfunction contours for a thick porous disk ($\varepsilon=1$) are presented in figure 5. Here, we see a rather pronounced flow splitting where fluid entering the disk for $r/R\gtrsim 0.55$ returns to the liquid film. The approximate solution where $\langle p\rangle_i$ is assumed to be a linear function of z does not capture the more complicated pressure contours given by the exact solution, nor will it predict the flow splitting that is shown in figures 6 and 7. From (2.10*b*) and (2.23), it is easy to show that $\langle v_z\rangle_s(r,\delta)>0$ for $0\leqslant r\leqslant R$, which means that for configuration (i), fluid within the porous disk never flows back into the liquid film. For configuration (ii), however, flow splitting becomes more pronounced with decreasing Υ and vanishes only in the limit $\varepsilon\to 0$.

It is of interest to examine the rate at which the liquid flows into the porous disk relative to the rate at which it flows from the liquid film at $r=R$. To examine this quantitatively, we consider the fraction of liquid from the film that flows into the porous disk for constant squeeze velocity $-\dot{\delta}$, which is defined as

$$\Phi=-\frac{1}{\dot{\delta}}\frac{2}{R^2}\int_0^R\langle v_z\rangle_s(r,\delta)r\,\mathrm{d}r=\frac{\kappa}{\mu\dot{\delta}}\frac{2}{R^2}\int_0^R\frac{\partial\langle p\rangle_i}{\partial z}(r,\delta)r\,\mathrm{d}r,\tag{3.2}$$

https://doi.org/10.1017/jfm.2018.635 Published online by Cambridge University Press

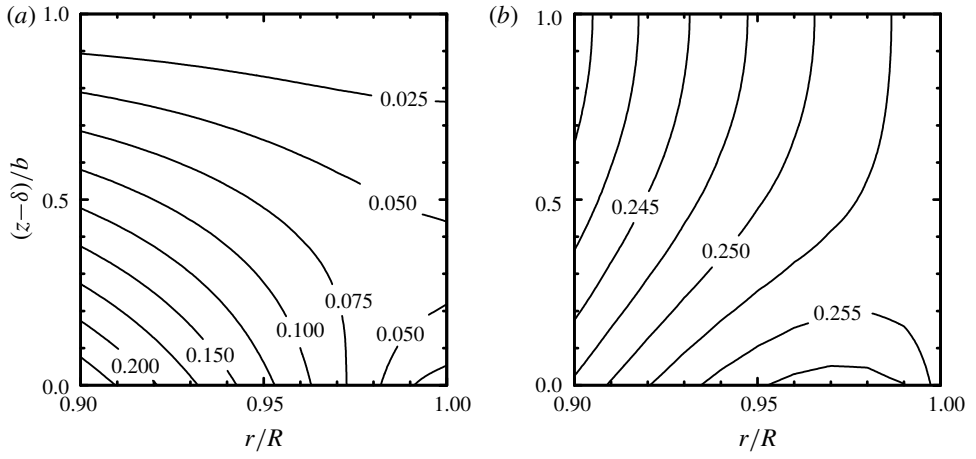


FIGURE 6. Detailed view of pressure (*a*) $-\langle p\rangle_i\delta^3/\mu\dot{\delta}R^2$ from (2.38) and streamfunction (*b*) $-\langle\psi\rangle_s/\dot{\delta}R^2$ from (2.40) contours in a porous disk for configuration (ii) with constant squeezing velocity $-\dot{\delta}$ for permeability parameter $\Upsilon=\kappa R/\delta^3=0.1$ with $\varepsilon=0.1$, $\delta/R=0.01$ and $\sigma=0$.

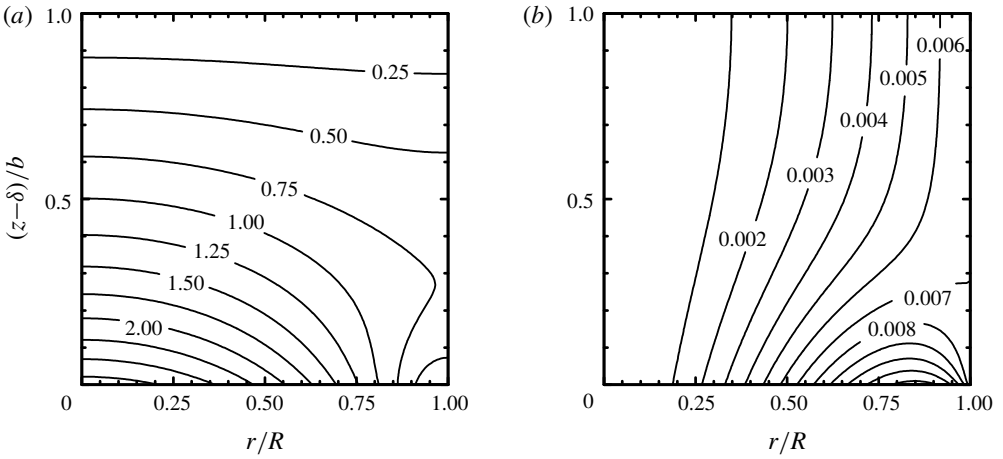


FIGURE 7. Pressure (*a*) $-\langle p\rangle_i\delta^3/\mu\dot{\delta}R^2$ from (2.38) and streamfunction (*b*) $-\langle\psi\rangle_s/\dot{\delta}R^2$ from (2.40) contours in a porous disk for configuration (ii) with constant squeezing velocity $-\dot{\delta}$ for permeability parameter $\Upsilon=\kappa R/\delta^3=0.1$ with $\varepsilon=1$, $\delta/R=0.01$ and $\sigma=0$.

where the second equality follows using (2.10*b*). The fraction of liquid that flows, or is squeezed, out of the film at $r=R$ is $1-\Phi$; for the case of an impermeable disk, $\Phi=0$. The dependence of Φ on Υ for configurations (i) and (ii) is shown in figure 8. For constant squeeze velocity $-\dot{\delta}$, since the film thickness δ decreases (Υ increases), Φ increases during squeezing. In figure 8 we see for a thin porous disk ($\varepsilon=0.1$) that Φ is larger for configuration (ii) compared with configuration (i), and the opposite is true for a thick porous disk ($\varepsilon=1.0$). This is explained by the fact that increasing the disk thickness for configuration (ii) leads to a larger resistance for flow to the reservoir, while for configuration (i) an increase in ε lowers the resistance for flow out of the

https://doi.org/10.1017/jfm.2018.635 Published online by Cambridge University Press

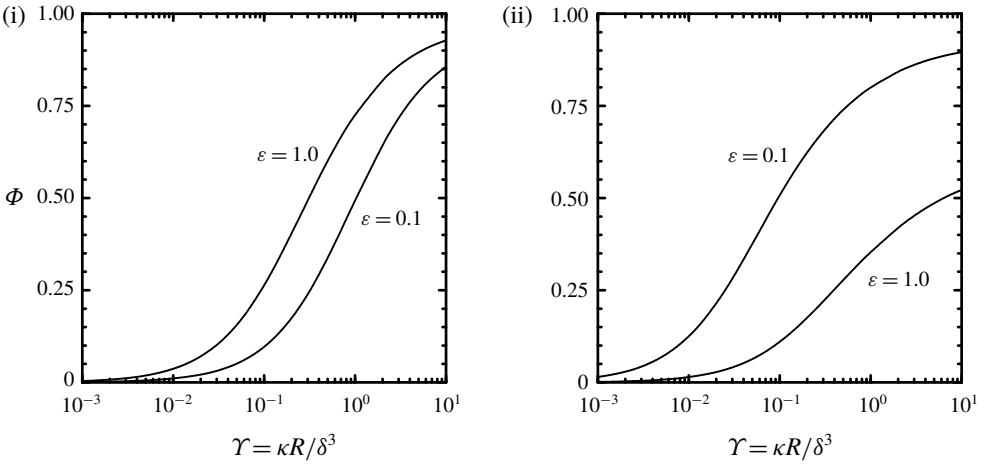


FIGURE 8. Fraction of liquid from the film that flows into the porous disk as defined in (3.2) for configurations (i) and (ii) with constant squeezing velocity $-\dot{\delta}$ as a function of permeability parameter $\Upsilon = \kappa R/\delta^3$ for $\sigma = 0$ and $\delta/R = 0.01$.

disk at $r = R$. Figure 8 also shows that the dependence of Φ on disk thickness ε is stronger for configuration (ii) compared to (i). As we have just seen (see figures 6 and 7), the degree of flow separation and flow from the porous disk back into the film ($\langle v_z \rangle_s(r, \delta) < 0$) for configuration (ii) increases with increasing ε.

As noted in the previous section, the sealed-edge configuration (ii) includes the case of an externally pressurized bearing where the mass flow rate $\mathcal{W}$ from the reservoir to the porous disk is prescribed. Figure 9 shows the pressure and radial velocity fields in the liquid film for the case of a constant film thickness ($\dot{\delta} = 0$). From this figure we again see that the pressure profile flattens and radial velocity decreases as Υ increases (see figure 4). Pressure and streamfunction contours within the porous disk for this case are presented in figure 10, which shows that the pressure field varies primarily in the axial direction leading to a flow in the axial direction. The modification of the lubricated squeezing flow technique for generating equibiaxial deformations in polymer melts (Venerus *et al.* 2010) is based on this type of flow where the liquid (lubricant) film thickness is constant.

3.2. *Load-bearing behaviour*

It is of great interest to understand the load-bearing behaviour of porous-walled thrust bearings and its dependence on the properties of the porous disk. The force exerted on the permeable disk $\mathcal{F}$ is due to the pressure field that develops in the liquid film, which is required to drive flow in the radial direction. As a reference, we consider the impermeable disk case ($\sigma = \Upsilon = 0$). For this case, expressions for $\mathcal{F}$ for configurations (i) and (ii) given in (2.26) and (2.43), respectively, simplify to

$$\frac{2\mathcal{F}}{3\mu\pi R^4} = -\frac{\dot{\delta}}{\delta^3}. \tag{3.3}$$

For constant squeezing velocity $-\dot{\delta}$, we see that $\mathcal{F} \to \infty$ as $\delta \to 0$.

Figure 11 shows the dependence of force on the porous disk $\mathcal{F}$ on the permeability parameter Υ for the sealed-face configuration (i). According to (3.3), we see that $\mathcal{F}$

https://doi.org/10.1017/jfm.2018.635 Published online by Cambridge University Press

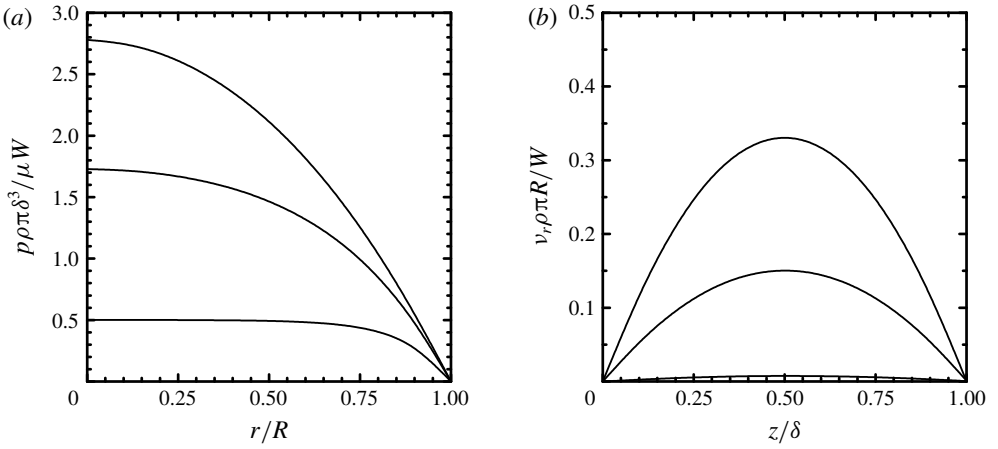


FIGURE 9. Pressure (a) from (2.36) and radial velocity at $r/R = 0.5$ (b) from (2.39) for configuration (ii) with constant $\mathcal{W}$ and $\dot{\delta} = 0$ for permeability parameter $\Upsilon = \kappa R/\delta^3 = 0.01$, 0.1, 1.0 (solid lines top to bottom) with $\varepsilon = 0.1$, $\delta/R = 0.01$ and $\sigma = 0$.

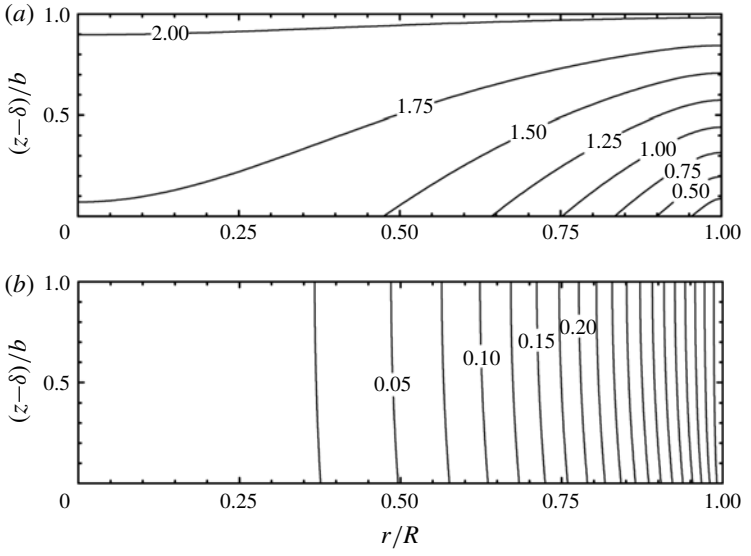


FIGURE 10. Pressure (a) $\langle p\rangle_i \rho\pi\delta^3/\mu\mathcal{W}$ from (2.38) and streamfunction (b) $\langle\psi\rangle_s \rho\pi/\mathcal{W}$ from (2.40) contours in a porous disk for configuration (ii) with constant $\mathcal{W}$ and $\dot{\delta} = 0$ for permeability parameter $\Upsilon = \kappa R/\delta^3 = 0.1$ with $\varepsilon = 0.1$, $\delta/R = 0.01$ and $\sigma = 0$.

is reduced relative to the impermeable disk case. The load-bearing capacity is further reduced by slip as shown by the dependence of $\mathcal{F}$ on σ. Results for the sealed-edge configuration (ii) with $p_0 = 0$ are presented in figure 12, where it is evident that $\mathcal{F}$ is also reduced relative to the impermeable disk case and is further reduced by slip. Comparison of figures 11 and 12 shows that, for a thin porous disk $\varepsilon = 0.1$, the load-bearing capacity of configuration (ii) is smaller than configuration (i). For example, for $\Upsilon = 1$, the load-bearing capacity of configuration (ii) is roughly a factor of 10 smaller than configuration (i). The dependence of $\mathcal{F}$ on Υ in these figures can be

https://doi.org/10.1017/jfm.2018.635 Published online by Cambridge University Press

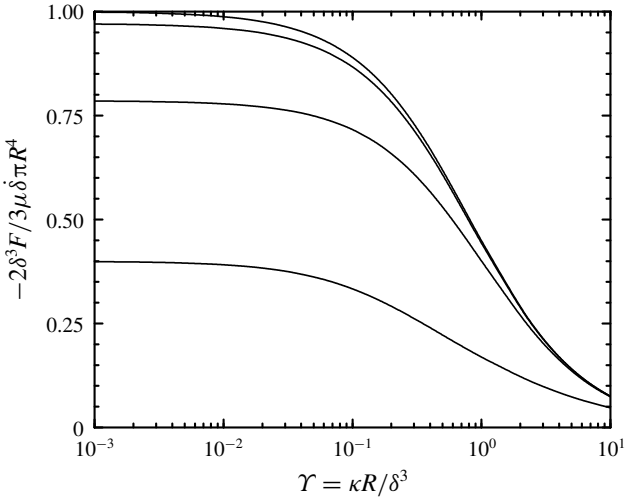


FIGURE 11. Force on porous disk from (2.26) for configuration (i) with constant squeezing velocity $-\dot{\delta}$ as a function of permeability parameter $\Upsilon = \kappa R/\delta^3$ for different values of slip parameter $\sigma = \sqrt{\kappa}/\delta\alpha = 0,\ 0.01,\ 0.1,\ 1.0$ (solid lines top to bottom) with $\varepsilon = 0.1$ and $\delta/R = 0.01$.

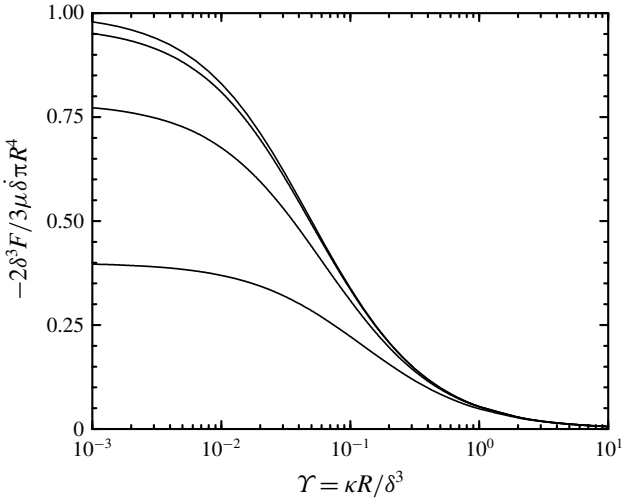


FIGURE 12. Force on porous disk from (2.43) for configuration (ii) with constant squeezing velocity $-\dot{\delta}$ as a function of permeability parameter $\Upsilon = \kappa R/\delta^3$ for different values of slip parameter $\sigma = \sqrt{\kappa}/\delta\alpha = 0,\ 0.01,\ 0.1,\ 1.0$ (solid lines top to bottom) with $\varepsilon = 0.1$ and $\delta/R = 0.01$.

understood when one considers the results in figure 8, which show that increasing Υ leads to an increase in Φ, thereby reducing the radial velocity (and pressure) in the liquid film.

The load-bearing behaviours of configurations (i) and (ii) for a thick porous disk ($\varepsilon = 1$) are presented in figure 13. A comparison of these results with those in figures 11 and 12 indicates that increasing ε leads to a reduction in the load-bearing

https://doi.org/10.1017/jfm.2018.635 Published online by Cambridge University Press

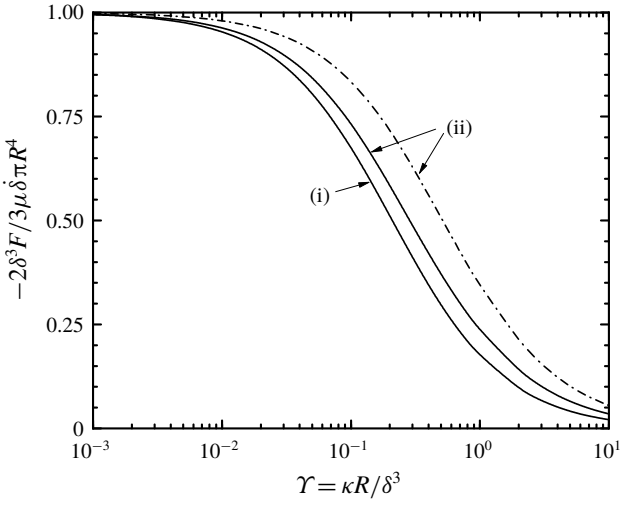


FIGURE 13. Force on porous disk from (2.26) for configuration (i) and from (2.43) for configuration (ii) with constant squeezing velocity $-\dot{\delta}$ as a function of permeability parameter $\Upsilon = \kappa R/\delta^3$ for $\sigma = 0$ with $\varepsilon = 1.0$ and $\delta/R = 0.01$. The dashed curve is the approximate solution for configuration (ii) given in (3.4).

capacity for configuration (i) and an increase in the load-bearing capacity for configuration (ii). The latter is explained by the fact that for configuration (ii) the flow is primarily in the axial direction and an increase in porous disk thickness requires a larger pressure in the liquid film to drive the flow. For configuration (i), an increase in disk thickness moves the impermeable upper surface away from the liquid film, thereby decreasing the pressure required to drive flow through the porous disk at permeable external surfaces. The load-bearing capacities of configurations (i) and (ii) coincide for $\varepsilon \approx 0.6$.

An expression for $\mathcal{F}$ using the approximate solution described above is obtained by substitution of (3.1) in (2.14) leading to

$$\frac{2\mathcal{F}}{3\mu\pi R^4} = -\frac{\dot{\delta}}{\delta^3}\frac{2\varepsilon}{3\Upsilon}\left[1 - \frac{2\mathrm{I}_1(\sqrt{12\Upsilon/\varepsilon})}{\sqrt{12\Upsilon/\varepsilon}\,\mathrm{I}_0(\sqrt{12\Upsilon/\varepsilon})}\right], \tag{3.4}$$

which is equivalent to the expression given by Verma (1980). For thin porous disks $\varepsilon \ll 1$, predictions for $\mathcal{F}$ from (3.4) are consistent with those from the exact solution in (2.43). However, as shown in figure 13 for $\varepsilon = 1$, the expression in (3.4) from the approximate model significantly over-predicts $\mathcal{F}$.

We now examine the dynamics of liquid-film thinning for constant applied force $\mathcal{F}$. Again, we use the impermeable case as a reference. Integration of (3.3) with $\delta(0) = \delta_0$ gives

$$\frac{\delta}{\delta_0} = \frac{1}{\sqrt{1 + 4\mathcal{F}\delta_0^2 t/3\mu\pi R^4}}, \tag{3.5}$$

which shows that $\delta \to 0$ only for $t \to \infty$. Figure 14 shows the liquid-film thickness as a function of time for configurations (i) and (ii) without a slip velocity ($\sigma = 0$) for different values of the permeability parameter $\Upsilon = \kappa R/\delta_0^3$. These results were obtained by a straightforward numerical integration of (2.26) and (2.43) with $\delta(0) = \delta_0$. As

https://doi.org/10.1017/jfm.2018.635 Published online by Cambridge University Press

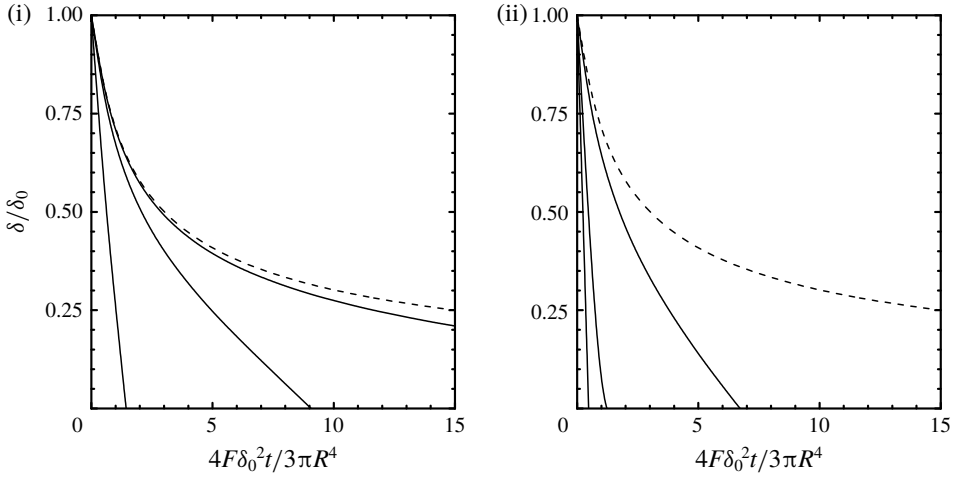


FIGURE 14. Liquid-film thickness as a function of time from (2.26) for configuration (i) and from (2.43) for configuration (ii) with constant squeezing force $\mathcal{F}$ for different values of permeability parameter $\Upsilon = \kappa R/\delta_0^3 = 0.01,\ 0.1,\ 1.0$ (solid lines top to bottom) with $\varepsilon = 0.1$, $\delta_0/R = 0.01$ and $\sigma = 0$. The dashed line is for the impermeable disk given by (3.5).

expected the rate of liquid-film drainage is increased relative to the impermeable case, and, for $\varepsilon = 0.1$, the rate of drainage is larger for configuration (ii) compared to configuration (i). Including a slip velocity ($\sigma \neq 0$) decreases $\mathcal{F}$ (see figures 11 and 12) and would further increase the rate of liquid film drainage. From figure 14 we see that complete drainage of the liquid film occurs at a finite time, which we denote as t_f: $\delta(t_f) = 0$. The dependence of t_f on the permeability parameter $\Upsilon = \kappa R/\delta_0^3$ for configurations (i) and (ii) for $\varepsilon = 0.1,\ 1$ is shown in figure 15. As expected, t_f decreases with increasing permeability Υ, which was previously reported for configuration (i) (Murti 1974*b*; Knox *et al.* 2015). For configuration (i) we see that increasing the thickness of the porous disk ε decreases the time for complete film drainage, while for configuration (ii) increasing ε leads to an increase in t_f. Also shown in figure 15 is t_f from the approximate solution for configuration (ii) determined by numerical integration of (3.4), which over-predicts t_f for the thicker porous disk $\varepsilon = 1$.

Finally, we consider the load-bearing characteristics of configuration (ii) when the liquid mass flow rate $\mathcal{W}$ from the reservoir to the porous disk is prescribed, or an externally pressurized bearing. This allows for a thrust bearing where the liquid film thickness can be controlled. Figure 16 shows the dependence of the load-bearing capacity on the permeability parameter Υ for constant $\mathcal{W}$ with constant liquid-film thickness ($\dot{\delta} = 0$). From this figure we see that $\mathcal{F}$ decreases with increasing disk permeability Υ and that a slip velocity further reduces load-bearing capacity. While $\mathcal{F}$ increases with decreasing Υ, the reservoir pressure p_0, which can be computed from (2.37), increases.

When operated with a prescribed liquid mass flow rate, the thrust bearing can also be used to lift an applied load. To demonstrate this, (2.41) is numerically integrated with the initial condition $\delta(0) = 0$; the constant applied force $\mathcal{F}$ is set by the expression in (2.41) at steady state ($\ddot{\delta} = 0$) and depends on the final liquid-film thickness $\delta(t \to \infty) = \delta_\infty$. As shown in figure 17, prescribing a constant $\mathcal{W}$ causes

https://doi.org/10.1017/jfm.2018.635 Published online by Cambridge University Press

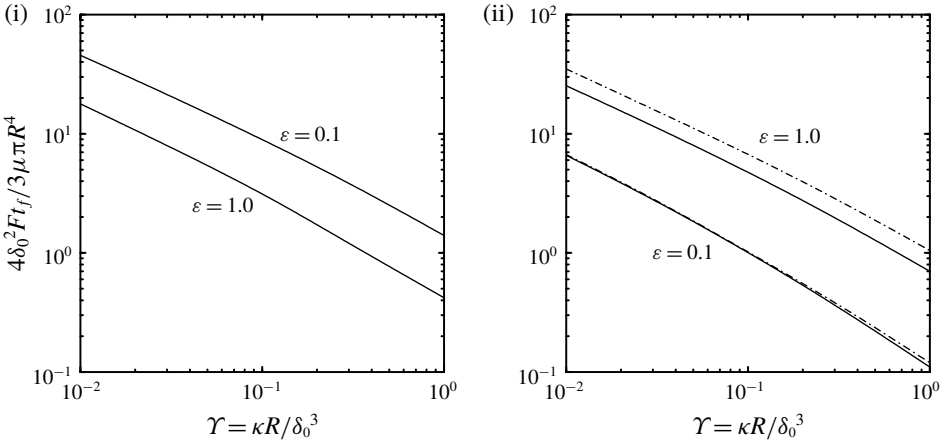


FIGURE 15. Time for complete drainage of liquid-film thickness $\delta(t_f) = 0$ for configurations (i) and (ii) with constant squeezing force $\mathcal{F}$ as a function of permeability parameter $\Upsilon = \kappa R/\delta_0^3$ with $\varepsilon = 0.1$, 1.0, $\delta_0/R = 0.01$ and $\sigma = 0$. The dot-dashed line is for the approximate solution from (3.4).

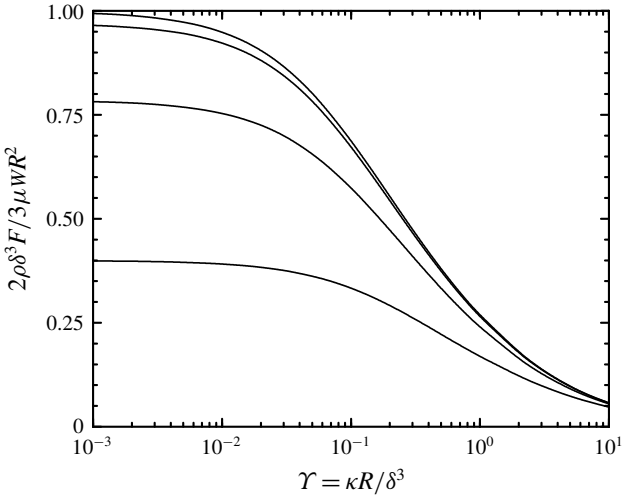


FIGURE 16. Force on porous disk from (2.41) for configuration (ii) with constant $\mathcal{W}$ and $\dot{\delta} = 0$ as a function of permeability parameter $\Upsilon = \kappa R/\delta^3$ for different values of slip parameter $\sigma = \sqrt{\kappa}/\delta\alpha = 0$, 0.01, 0.1, 1.0 (solid lines top to bottom) with $\varepsilon = 0.1$ and $\delta/R = 0.01$.

the liquid-film thickness to increase, lifting the load, to the final liquid-film thickness δ_∞. Alternatively, one could examine the time evolution of the film thickness if the reservoir pressure p_0 were prescribed, and $\mathcal{W}$ would be determined by (2.37).

4. Summary

Squeeze flows in liquid films bound by a porous disk have been investigated for two configurations (see figure 1). In the sealed-face configuration (i), the upper surface of

https://doi.org/10.1017/jfm.2018.635 Published online by Cambridge University Press

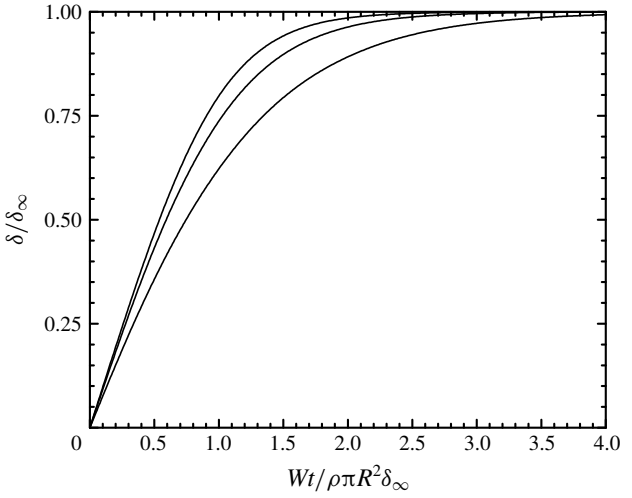


FIGURE 17. Liquid-film thickness as a function of time by integration of (2.41) for configuration (ii) with constant $\mathcal{W}$ for different values of permeability parameter $\Upsilon = \kappa R/\delta_\infty^3 = 0.001$, 0.01, 0.1 (solid lines top to bottom) with $\varepsilon = 0.1$, $\delta_\infty/R = 0.01$ and $\sigma = 0$. The squeezing force $\mathcal{F}$ is determined from figure 17 with $\delta \to \delta_\infty$.

the porous disk is impermeable and in the sealed-edge configuration (ii), the upper surface of this disk is permeable and exposed to a reservoir having uniform pressure. For configuration (ii), it is possible to control the flow of liquid from the reservoir to the porous disk, or to allow liquid to flow out of the porous disk to the reservoir at ambient pressure making it similar to configuration (i). Analytical solutions of the coupled systems of equations governing flow in the porous disk (Darcy's law) and liquid film (lubrication approximation) are obtained for both configurations leading to expressions for velocity and pressure fields as well as the force exerted on the porous disk.

Results have been obtained as a function of three dimensionless parameters that are determined by the disk permeability (Υ) and geometry (ε) and by a slip velocity (σ) at the interface between the porous disk and liquid film. Velocity and pressure fields in the liquid film are qualitatively the same in both configurations, while in the porous disk they can be qualitatively different under certain conditions. In particular, we show that for configuration (ii) where the reservoir is at ambient pressure, flow in the porous disk exhibits a stagnation point and flow separation where a portion of the liquid in the film flows into the porous disk and then back into the film. The fraction of the liquid in the film that flows through the porous disk (as opposed to being squeezed out of the liquid film) has a strong dependence on disk permeability (Υ) and geometry (ε) with a qualitatively different dependence on the latter for configurations (i) and (ii).

The load-bearing capacity of configuration (i) and configuration (ii) with the reservoir at ambient pressure have been examined as a function of disk permeability and geometry and the magnitude of a slip velocity. The dependence on disk permeability (Υ) is qualitatively similar for the two configurations, while the dependence on porous disk thickness (ε) is qualitatively different. In fact, we find that the load-bearing capacity of the two configurations with the same permeability is equal for a particular value of disk thickness. The presence of a slip velocity leads to a significant reduction in the load-bearing capacity for both configurations. We also

https://doi.org/10.1017/jfm.2018.635 Published online by Cambridge University Press

demonstrate the range of applicability for predicting load-bearing capacity obtained from a previously published approximate model for configuration (ii). The dynamics of liquid-film thickness for a constant applied load has been investigated. We find that the time for the film thickness to vanish decreases with increasing disk permeability (Υ) for both configurations (i) and (ii); it decreases with increasing disk thickness (ε) for configuration (i), and shows the opposite trend for configuration (ii). Finally, we have shown for configuration (ii) with a prescribed mass flow from the reservoir, that the liquid-film thickness can be controlled allowing the bearing to lift a constant load.

The results presented here have important consequences with regard to the design of thrust bearings where load-bearing characteristics can be tuned by appropriate choices of disk permeability and geometry. These results are also relevant to understanding the behaviour of diathrodial joints and approaches for their treatment and/or replacement.

REFERENCES

ATESHIAN, G. A. 2009 The role of interstitial fluid pressurization in articular cartilage lubrication. *J. Biomech.* **42**, 1163–1176.

BEAVERS, G. S. & JOSEPH, D. D. 1967 Boundary conditions at a naturally permeable wall. *J. Fluid Mech.* **30**, 197–207.

CHATRAEI, S. H., MACOSKO, C. W. & WINTER, H. H. 1981 Lubricated squeezing flow: a new biaxial extensional rheometer. *J. Rheol.* **25**, 433–443.

COUSSOT, P. 2014 Yield stress fluid flows: a review of experimental data. *J. Non-Newtonian Fluid Mech.* **211**, 31–49.

ELSHARKAWY, A. A. & NASSAR, M. M. 1996 Hydrodynamic lubrication of squeeze-film porous bearings. *Acta Mech.* **118**, 121–134.

ENGMANN, J., SERVAIS, C. & BURBIDGE, A. S. 2005 Squeeze flow theory and applications to rheometry: a review. *J. Non-Newtonian Fluid Mech.* **132**, 1–27.

GUADARRAMA-MEDINA, T., SHIU, T.-Y. & VENERUS, D. C. 2009 Direct comparison of equibiaxial elongational viscosity measurements from lubricated squeezing flow and MultiAxiales Dehnrheometer. *Rheol. Acta* **48**, 11–17.

HAMROCK, B. J., SCHMID, S. R. & JACOBSON, B. O. 2004 *Fundamentals of Fluid Film Lubrication*. Marcel Dekker.

HAMZA, E. A. & MACDONALD, D. A. 1981 A fluid film squeezed between two parallel plane surfaces. *J. Fluid Mech.* **109**, 147–160.

HOU, J. S., MOW, V. C., LAI, W. M. & HOLMES, M. H. 1992 An analysis of the squeeze-film lubrication mechanism for articular cartilage. *J. Biomech.* **25**, 247–259.

JACKSON, J. D. 1963 A study of squeezing flow. *Appl. Sci. Res.* **11**, 148–152.

KARMAKAR, T. & SEKHAR, G. P. R. 2018 Squeeze-film flow between a flat impermeable bearing and an anisotropic porous bed. *Phys. Fluids* **30**, 043604.

KNOX, D. J., DUFFY, B. R., MCKEE, S. & WILSON, S. K. 2017 Squeeze-film flow between a curved impermeable bearing and a flat porous bed. *Phys. Fluids* **29**, 023101.

KNOX, D. J., WILSON, S. K., DUFFY, B. R. & MCKEE, S. 2015 Porous squeeze-film flow. *IMA J. Appl. Maths* **80**, 376–409.

KOMPANI, M. & VENERUS, D. C. 2000 Equibiaxial extensional flow of polymer melts via lubricated squeezing flow. Part 1. Experimental analysis. *Rheol. Acta* **39**, 444–451.

KUZMA, D. C. 1967 Fluid inertia effects in squeezed films. *Appl. Sci. Res.* **18**, 15–20.

LIN, J.-R. 1996 Viscous shear effects on the squeeze-film behavior in porous circular disks. *Intl J. Mech. Sci.* **38**, 373–384.

LIN, J.-R., LU, R.-F. & YANG, C.-B. 2001 Derivation of porous squeeze-film Reynolds equations using the Brinkman model and its application. *J. Phys.* D **34**, 3217–3223.

METEEN, G. H. 2002 Constant-force squeeze flow of soft solids. *Rheol. Acta* **41**, 557–566.

https://doi.org/10.1017/jfm.2018.635 Published online by Cambridge University Press

MICK, R. M., SHIU, T.-Y. & VENERUS, D. C. 2015 Equibiaxial elongational viscosity measurements of commercial polymer melts. *Polym. Engng Sci.* **55**, 1012–1017.

MICK, R. M. & VENERUS, D. C. 2017 A novel technique for conducting creep experiments in equibiaxial elongation. *Rheol. Acta* **56**, 591–596.

MURTI, P. R. K. 1974*a* Effect of velocity slip in an externally pressurized porous thrust bearing working with an incompressible fluid. *J. Appl. Mech.* **43**, 404–408.

MURTI, P. R. K. 1974*b* Squeeze-film behavior in porous circular disks. *J. Lubr. Tech.* **96**, 206–209.

NABHANI, M., KHLIFI, M. E. & BOU-SAÏD, B. 2010 A general model for porous medium flow in squeezing film situations. *Lubr. Sci.* **22**, 37–52.

PRAKASH, J. & VIJ, S. K. 1974 Effect of velocity slip on porous-walled squeeze films. *Wear* **29**, 363–372.

REYNOLDS, O. 1886 On the theory of lubrication and its application to Mr Beauchamp Tower's experiments, including an experimental determination of the viscosity of olive oil. *Phil. Trans. R. Soc. Lond.* **177**, 157–234.

SPARROW, E. M., BEAVERS, G. S. & HUANG, I. T. 1972 Effects of velocity slip on porous-walled squeeze flows. *J. Lubr. Tech.* **94**, 260–264.

STEFAN, J. 1874 Versuche über die scheinbare Adhäsion. *Sitz. Kais. Akad. Wiss. Math. Nat. Wien* **69**, 713–735.

VENERUS, D. C., KOMPANI, M. & BERNSTEIN, B. 2000 Equibiaxial extensional flow of polymer melts via lubricated squeezing flow. Part 2. Flow modeling. *Rheol. Acta* **39**, 574–582.

VENERUS, D. C., SHIU, T.-Y., KASHYAP, T. & HOSTTETLER, J. 2010 Continuous lubricated squeezing flow: a novel technique for equibiaxial elongational viscosity measurements on polymer melts. *J. Rheol.* **54**, 1083–1095.

VERMA, R. L. 1980 Effect of velocity slip in an externally pressurized porous circular thrust bearing. *Wear* **63**, 239–244.

WHITAKER, S. 1999 *The Method of Volume Averaging*. Kluwer Academic.

WU, H. 1970 Squeeze-film behavior for porous annular disks. *J. Lubr. Tech.* **92**, 593–596.

YOUSEFI, M., BOU-SAÏD, B. & TICHY, J. 2015 Axisymmetric squeezing of a Phan-Thien and Tanner lubricant film under imposed constant load in the presence of a poroelastic medium. *Lubr. Sci.* **27**, 505–522.

https://doi.org/10.1017/jfm.2018.635 Published online by Cambridge University Press